

Manuscript Template

Nanowrinkled Carbon Aerogels Embedded with FeN_x Sites as Effective Oxygen Electrodes for Rechargeable Zinc-Air Battery

Ting He,^{1,2,†} Bingzhang Lu,^{2,†} Yang Chen,¹ Yong Wang,¹ Yaqiang Zhang,³ John L. Davenport,⁴ Alan P. Chen,⁴ Chih-Wen Pao,⁵ Min Liu,⁶ Zhifang Sun,¹ Alexander Stram,⁴ Alexander Mordaunt,⁴ Jairo Velasco Jr.,⁴ Yuan Ping,² Yi Zhang,^{1,7,*} Shaowei Chen^{2,*}

- ¹ State Key Laboratory for Powder Metallurgy, College of Chemistry and Chemical Engineering, Central South University, Changsha 410083 (China)
- ² Department of Chemistry and Biochemistry, University of California, 1156 High Street, Santa Cruz, California 95064 (United States)
- ³ Department of Chemical and Materials Engineering, University of Alberta, Edmonton, Alberta T6G 1H9 (Canada)
- ⁴ Department of Physics, University of California, 1156 High Street, Santa Cruz, California 95064 (United States)
- ⁵ X-ray Absorption Group, National Synchrotron Radiation Research Center, Hsinchu 30076 (Taiwan)
- ⁶ Institute of Super-Microstructure and Ultrafast Process in Advanced Materials, School of Physics and Electronics, Central South University, Changsha 410083 (China)
- ⁷ Key Laboratory of Materials Processing and Mold (Zhengzhou University), Ministry of Education, Zhengzhou 450002 (China)
- * Corespondence should be address to Yi Zhang: yzhangcsu@csu.edu.cn; Shaowei Chen: shaowei@ucsc.edu.
- † These authors contributed equally to this work.

Abstract

Rational design of single metal atom sites in carbon substrates by a flexible strategy is highly desired for the preparation of high-performance catalysts for metal-air batteries. In this study, biomass hydrogel reactors are utilized as structural templates to prepare carbon aerogels embedded with single iron atoms by controlled pyrolysis. The tortuous and interlaced hydrogel chains lead to the formation of abundant nanowrinkles in the porous carbon aerogels, and single iron atoms are dispersed and stabilized within the defective carbon skeletons. X-ray absorption spectroscopy measurements indicate that the iron centers are mostly involved in the coordination structure of FeN₄, with a minor fraction (ca. 1/5) in the form of FeN₃C. First-principles calculations show that the FeN_x sites in the Stone-Wales configurations induced by the

nanowrinkles of the hierarchically porous carbon aerogels show a much lower free energy than the normal counterparts. The resulting iron and nitrogen-codoped carbon aerogels exhibit excellent and reversible oxygen electrocatalytic activity, and can be used as bifunctional cathode catalysts in rechargeable Zn–air batteries, with a performance even better than that based on commercial Pt/C and RuO $_2$ catalysts. Results from this study highlight the significance of structural distortions of the metal sites in carbon matrices in the design and engineering of highly active single atom catalysts.

MAIN TEXT

1. Introduction

Climate change and environmental pollution have motivated the development of sustainable, clean energy technologies, of which rechargeable metal-air batteries have drawn tremendous attention owing to their high energy density and minimal impacts on the environment.[1-4] The overall efficiency of the charge-discharge process of metal-air batteries is determined by two major reactions, oxygen reduction reaction (ORR) and oxygen evolution reaction (OER). Although platinum group metal (PGM) materials, such as Pt/C, RuO₂, and Ir/C, possess excellent catalytic activity for either ORR or OER, none of these noble metal catalysts displays a satisfactory performance for both,[5] and their scarcity and high costs greatly hinder their practical applications.[6, 7] Therefore, development of bifunctional catalysts with a low cost and high activity is of both fundamental and technological significance, but remains a great challenge.

Recent studies have demonstrated that PGM-free nanocomposites based on carbon materials, such as heteroatom (including non-metal and metal atoms) doped porous carbon, are promising bifunctional oxygen catalysts.[8-10] In fact, transition metal-doped carbon catalysts have been widely investigated due to the unique chemical properties caused by their adjustable 3d electronic orbitals. In particular, transition metal-based single atom catalysts display overwhelming superiority as compared to their nanoparticle and nanocluster counterparts.[11-15] For instance, single-site dispersion of FeN_x species in a two-dimensional nitrogen-doped porous carbon layer has been found to exhibit a remarkable catalytic activity toward both ORR and OER in alkaline media,[1] where a range of catalytic active sites have been proposed, such as CoN₂C₂, FeN₃C, FeN₄ and FeN₄O.[16-18] However, the effects of structural distortion induced by the single metal sites on the catalytic activity have long been ignored although such structural defects are common in carbon.

Herein, biomass hydrogels (i.e., chitosan, gelatin, and agar), which have long been known for their diverse applications and economic advantages, [19, 20] were prepared and used as unique precursors, templates and reactors to produce three-dimensional, nanowrinkled carbon aerogels embedded with FeN_x single sites. [21-23] Due to the abundant functional groups on the hydrogel chains, defective single metal sites were dispersed and stabilized within the nanowrinkled, porous carbon aerogels. First-principles calculations showed that the FeN_x sites in the Stone-Wales configurations induced by the carbon nanowrinkles displayed a much lower free energy for oxygen electrocatalysis than the normal counterparts. Electrochemical measurements exhibited apparent and reversible oxygen electrocatalytic performance towards both ORR and OER. When the nanowrinkled carbon aerogels were used as the air-cathode of a zinc-air battery, the battery displayed a higher open circuit voltage, higher energy

density as well as better cycling stability than that with commercial Pt/C-RuO₂ catalysts.

2. Results and Discussion

Synthesis and characterization

In this study, flexible biomass hydrogels were synthesized in a facile process and employed as 3D templates to prepare carbon aerogels embedded with single metal atoms (Figure 1a and S1). In order to achieve atomic dispersion, the hydrogel networks were modified by two strategies to minimize metal aggregation. The first is "headstream fixation", which means immobilization of metal atoms into the hydrogel reactor by complexation agents (e.g., phenanthroline, PM); and the other, "roadblocks", is based on rigid templates, such as SiO₂ nanoparticles and Zn atoms. Experimentally, a variety of hydrogel/hydrosol networks, i.e., CSsi-Zn/FePM, CS_{Si}/FePM, CS_{Si}/Fe, and CS_{Si}, were prepared by using chitosan (CS) as the structural scaffold, along with a select combination of other precursors, such as SiO₂ nanoparticles (Si), FePM, and Zn salt (details in the Materials and Methods section). The morphological details were first investigated by scanning electron microscopy (SEM) measurements. From Figure S2, freeze-dried CSsi/FePM, CSsi/Fe and CSsi hydrosols can be seen to consist of uneven microcavities. However, as shown in Figure 1b, the microcavities of the CS_{Si-Zn}/FePM hydrogel shows a more uniform size of ca. 50 um, forming a 3D, continuous framework composed of intertwining CS-Zn chains. This suggests that Zn ions can induce the hydrogelation of CS hydrosol to form much more uniform 3D intertwining networks, which further facilitates the generation of nanowrinkles.[24] Circular dichroism (CD) and UV-vis absorption measurements were then carried out to monitor the structural evolution from CSsi sol to CSsi-zn/FePM hydrogel. As depicted in Figure S3a, the incorporation of both FePM and Zn²⁺ ions into chitosan led to marked conformational changes of the CS chains. In UV-vis absorption measurements (Figure S3b), two new peaks can be seen to emerge at ca. 226 nm and 268 nm, due to the strong complexation interaction between Fe and PM.[25]

The freeze-dried $CS_{Si-Zn}/FePM$ hydrogel was then used as a 3D reactor to synthesize metal-doped carbon aerogels by controlled pyrolysis, which was then subject to HF etching to remove the SiO_2 templates (Figure 1a), producing NCA_{C-Zn}/Fe (Figure 1c inset). Control samples of NCA_C/Fe , CA_C/Fe , and CA_C were prepared in a similar fashion (details in the Materials and Methods section). From the transmission electron microscopy (TEM) images in Figure S4, one can see that the NCA_{C-Zn}/Fe sample displays a highly porous, nanowrinkled structure with rich mesopores of ca. 10 nm in diameter. In both bright-field (Figure 1c) and dark-field (Figure 1d) scanning transmission electron microscopy (STEM) images, one can clearly see the formation of single metal atoms (red circles) embedded into the porous carbon matrix. The corresponding elemental maps clearly show that the C, N and Fe elements are homogeneously distributed across the aerogel (Figure 1e). These results indicate successful construction of N-doped carbon aerogels embedded with isolated Fe atoms by using biomass hydrogels as the reactors.

In order to examine the mechanical and electrical properties of the obtained porous carbon, Fast Force Mapping (FFM) measurements were then carried out. The data presented in Figure 1f-g and S5 exhibit a \sim 10 nm variation in the mechanical and electrical properties of the porous carbon, confirming the formation of nanowrinkled carbon. Domains dictated by round features in topography (Figure S5a) are outlined

by prominent changes in max force (Figure S5b), and an increase in the adhesion force (Figure 1f). Notably, the adhesion force, which represents the bulk modulus or stiffness of the sample, indicates that these round regions are stiffer in the center and softer around the edges. Typically, sp²-hybridized carbon exhibits hydrophobic characters, whereas defective carbons are more hydrophilic.[26, 27] With an AFM tip that consists of a hydrophilic silicon oxide layer, a high adhesion force corresponds to a hydrophilic domain. This implies that the metal centers are most likely situated within the high adhesion force areas. Interestingly, from Figure 1f-g, one can see that the soft nodes correspond to high electrical conductance. Taken together, these results suggest that the metal sites are mostly located in the high adhesion and high conductivity area of the porous carbon aerogel.[28, 29] Both features are conducive to oxygen electrocatalysis.

The porosity of the obtained samples was then quantitatively evaluated by N₂ adsorption-desorption measurements. The carbon aerogels obtained above all shows a Type IV isotherm (Figure 2a and S6a), which suggests the formation of a complex porous network containing a myriad of mesopores with an average size of ca. 10 nm, in line with the diameter of the SiO₂ nanoparticle.[30] From the isotherms, the specific surface area of NCA_{C-Zn}/Fe was estimated to be 609 m² g⁻¹, with a microporous surface area of 111 m² g⁻¹, which is the highest among the series, a condition favorable for the formation of abundant active sites (Figure S6b and Table S1). The corresponding Xray powder diffraction (XRD) patterns are shown in Figure S7, where only one broad peak at ca. 25° can be observed, due to the (002) diffraction of graphitic carbon.[31] This carbon diffraction became gradually sharpened from CSc to NCAc-zn/Fe, indicating an increasing degree of graphitization. Importantly, the fact that no other diffraction features were observed suggests the absence of metal (oxide) nanoparticles. In Raman measurements, the I_D/I_G ratio of NCA_{C-Zn}/Fe was estimated to be ca. 1.15, much higher than those of the control samples (Figure 2b), signifying the generation of rich defects which may be conducive to the formation of metal active sites. [31]

The elemental compositions of the obtained carbon samples were then quantitatively assessed by inductively coupled plasma atomic emission energy-dispersive spectroscopy spectroscopy (ICP-OES) and X-ray measurements. Results from ICP-OES analysis showed that the Fe content in the carbon aerogel was about 0.22 wt% for CAc/Fe, 0.61 wt% for NCAc/Fe, and 0.72 wt% for NCA_{C-Zn}/Fe, in good accordance with the EDS results (Figure S8, Table S2 and S3). The increased metal content suggests the important roles of PM (chelation) and Zn²⁺ ions (porogen and gel initiator) into fixing Fe centers in the carbon matrix. Further analysis was conducted with X-ray photoelectron spectroscopy (XPS) measurements. First of all, no Fe-O peak can be resolved in the high-resolution scan of the O 1s electrons (Figure S9a), suggesting that Fe atoms are most likely coordinated to other atomic sites such as N and C; and from the XPS spectra of the N 1s electrons of the series of samples (Figure 2c, S9b and S9c), one can see that the successive introduction of PM and Zn²⁺ into the precursors increased the N doping from 2.25 at% to 3.60 at% in the carbon matrix (Table S4 and S5), and the pyridinic N fraction was the highest in the NCA_C/Fe (0.52 at%) and NCA_{C-Zn}/Fe (0.51 at%) samples. In addition, as compared to CSc/Fe, the much stronger Fe-N peak (0.44 at% vs. 0.04 at%) in the NCAc-zn/Fe sample suggests the generation of more abundant FeNx moieties in the carbon aerogels.

The structural configuration of the FeN_x functional moiety was then examined by X-ray absorption spectroscopy (XAS) measurements. From Figure 2d, one can see that the Fe K-edge X-ray absorption near-edge spectrum (XANES) of NCA_{C-Zn}/Fe is very similar to that of FePc, but markedly different from that of a Fe foil, suggesting a comparable oxidation state (+2) of the Fe centers in NCA_{C-Zn}/Fe and FePc. In the extended X-ray absorption fine structure (EXAFS) spectrum of the Fe foil, the Fe–Fe peak is well-defined at 2.21 Å (Figure 2e); however, this peak is absent in NCA_{C-Zn}/Fe, consistent with the atomic dispersion of Fe in the NCA_{C-Zn}/Fe sample (Figure 1). In fact, both the NCA_{C-Zn}/Fe and FePc samples display only a single major peak at 1.41 Å, which can be assigned to the Fe–N bond. Furthermore, the first shell of NCA_{C-Zn}/Fe is well-fitted with 3.8 N and 0.2 C with the same bond length of 1.94 Å (Figure 2f and S10). Taken together, these results suggest that the Fe centers in NCA_{C-Zn}/Fe were mostly involved in the coordination structure of FeN₄, with a minor fraction (ca. 1/5) in the form of FeN₃C.

Theoretical investigation of the ORR using the NCAc-zn/Fe catalyst.

First-principles calculations were then carried out to shed light on the contributions of FeN₄ and FeN₃C moieties to the electrocatalytic activity. It is likely that the interlaced 3D structure of the hydrogel networks and the tortuous CS chains can lead to the formation of abundant wrinkles in the obtained porous carbon aerogels. Therefore, the electrocatalytic activity of Stone-Wales (SW)-defect FeN₄ (FeN₄ SW) and FeN₃C (FeN₃C SW) moieties, which can be formed by the nanowrinkles of carbon matrices, are examined by theoretical calculations. Figure 3a-b and S11 show the side view and top view of the atomic models of the four kinds of Fe-N centers. From the atomic models, one can see that the normal FeN₄ and normal FeN₃C moieties exhibit a planar structure in the carbon matrices, while FeN₄SW and FeN₃CSW show a distorted non-planar structure. The simulated scanning tunneling microscopic (STM) images of the FeN₄ and FeN₄ SW moieties are presented in Figure 3c-d and S12. As compared to normal FeN₄, the SW defects cause significant redistribution of electron densities of FeN₄ and adjacent carbon atoms. Figure 3e displays the total density of states (DOS) of normal and SW Fe-N centers. According to Figure 3f, for the FeN₄SW on a graphene sheet, the Fe atom makes the largest contributions to the DOS near the Fermi level (red peak), which is similar to that (black line) of normal FeN₄. Apparently, the marked state of FeN₄ SW (highlighted by arrows in Figure 3e) is much closer to the Fermi level than that of normal FeN₄, indicating a higher probability of donating electrons and reducing oxygen.

To evaluate the ORR activity of these Fe-N metal centers, the reaction free energy is calculated at the applied potential of +0.9 V vs RHE and plotted in Figure 3g. One can see that except for the fourth electron-transfer step, the first three electron-transfer steps are exothermic at +0.9 V, indicating that the rate determining step (RDS) is most likely the fourth electron-transfer step of water formation and desorption. In comparison with normal FeN₄ and FeN₃, both FeN₄ SW and FeN₃ SW show much lower endothermic energies (0.179 eV and 0.228 eV), implying a lower reaction overpotential. These results suggest that the nanowrinkles can enhance the electrocatalytic activity of Fe-N centers on the carbon matrices by forming SW defects, as manifested below in electrochemical tests.

Electrocatalytic activity toward ORR

The electrocatalytic activity of the nanowrinkled carbon aerogels obtained above was then investigated in 0.1 M KOH. First, electrical impedance spectroscopy (EIS) analysis was carried out to investigate the electron-transfer kinetics. For the NCA_{C-Zn}/Fe catalyst, the small diameter at high frequency and the steep tail at low frequency suggests excellent channels for both mass transfer and charge transfer. Such a low impedance is anticipated to facilitate ORR electrocatalysis (Figure S13). Figure 4a-b shows the ORR polarization curves and H₂O₂ yields of the carbon aerogels, in comparison to commercial Pt/C (20 wt%). As a metal-free catalyst, the CA_C sample shows a rather apparent electrocatalytic activity with an onset potential (Eonset) of +0.94 V vs RHE and half-wave potential ($E_{1/2}$) of +0.79 V, much more positive than those of other carbon catalysts reported in recent literature. [15, 32, 33] This suggests that biomass alone may be exploited as a carbon source to fabricate metal-free ORR electrocatalysts. Notably, doping of FePM complex into the CS_{Si} lead to a marked enhancement of the catalytic performance with E_{onset} = +1.10 V and $E_{1/2}$ = +0.90 V (NCA_{C-7n}/Fe), which is even better than those of commercial Pt/C (+0.99 V and +0.83V).[34] Likewise, the NCA_{C-Zn}/Fe single atom catalyst shows a lowest average H₂O₂ vield (1.45%) within the potential range of +0.2 V to +0.9 V, signifying a high-efficiency 4e⁻ reduction pathway (Figure S14-S16). From the Koutecky-Levich plots, the kinetic current density (I_k) at +0.85 V was estimated to be 9.12 mA cm⁻², about 3.3 times that of Pt/C (2.80 mA cm⁻², Figure 4c). Both NCA_{C-Zn}/Fe and Pt/C show a low Tafel slope (85 vs. 87 mV dec⁻¹) in the high potential range, illustrating an efficient kinetic process of ORR on these two catalysts (Figure 4d). Besides, in contrast with Pt/C, the NCAczn/Fe exhibits remarkable durability and methanol tolerance (Figure S16). In addition, the $E_{1/2}$ and diffusion-limited current density of the NCA_{C-Zn}/Fe were comparable to those of Pt/C in acidic media (0.1 M HClO₄), suggesting high ORR activity of the single iron atom catalysts even at low pH (Figure 4e).

To distinguish the contributions of the Fe center and adjacent non-metal atoms to the electrocatalytic activity, electrochemical measurements were then carried out with the addition of SCN- as the poisoning species. One can see that upon the addition of 10 mM SCN- into 0.1 M KOH, the $E_{1/2}$ of NCA_{C-Zn}/Fe exhibited a negative shift of 20 mV (Figure S17). The relatively mild performance deterioration suggests that in addition to the Fe sites, adjacent non-metal atoms also play a critical role in driving the catalytic reaction. This is actually in good agreement with the formation of FeN_x SW moieties in the carbon skeletons, where structural distortion leads to activation of adjacent C atoms (Figure 3 and S12).[8]

Notably, other biomass hydrogels, such as gelatin and agar, can also be used as templates to fabricate nanowrinkled carbon aerogels embedded with single metal atoms in a similar fashion. The resulting catalysts, NCA_{G-Zn}/Fe and NCA_{A-Zn}/Fe, both displayed excellent catalytic activities towards ORR in alkaline media, with an $E_{1/2}$ of +0.92 and +0.89 V, and E_{onset} of +1.12 and 1.10 V, respectively (Figure 4f and inset). These results highlight the universality of the synthetic strategy in the preparation of high-performance ORR electrocatalysts (Figure S1).

Electrocatalytic activity toward OER and Zinc-air battery performance

The electrocatalytic activity of the NCA_{C-Zn}/Fe aerogels towards OER was then examined and compared with commercial RuO₂ in 1 M KOH with iR correction. From Figure 5a, one can see that for NCA_{C-Zn}/Fe, an overpotential (η_{10}) of +370 mV was needed to achieve the current density of 10 mA cm⁻², a performance comparable to that (η_{10} = +340 mV) of commercial RuO₂. The NCA_{C-Zn}/Fe also exhibits a Tafel slope of

98 mV dec⁻², close to that of RuO₂ (71 mV dec⁻²), signifying a favorable OER kinetic (Figure S18). Thanks to the excellent electrocatalytic performance towards both ORR and OER, the NCA_{C-Zn}/Fe SACs shows a low potential difference (Δ E) of only 0.71 V between the OER potential at 10 mA cm⁻² (E_{OER,10}) and ORR potential at 3 mA cm⁻² (E_{ORR,3}), much smaller than those of bifunctional M–N–C catalysts reported recently in the literature.[*11*, *35*, *36*]

With such a remarkable bifunctional performance, the NCA_{C-Zn}/Fe aerogels was tested as the air-cathode for a Zn-air battery, in comparison with that using commercial Pt/C-RuO₂ mixture (mass ratio 1:1), along with a Zn plate as the anode. From Figure 5b-c, the NCAc-zn/Fe Zn-air battery can be seen to show an open circuit voltage (OCV) of 1.50 V and a maximum power density of 231 mW cm⁻², about 6 mV and 20 mW cm⁻² higher than those of the Pt/C-RuO₂ counterpart. Figure 5d shows the corresponding constant current discharge tests at various current densities (5, 10, 20 and 50 mA cm⁻²) of the two batteries. One can see that the NCA_{C-Zn}/Fe-Zn battery exhibited a much higher discharge voltage within a wide range of current density (5 to 50 mA cm⁻²). At the constant current density of 10 mA cm⁻², the NCA_{C-Zn}/Fe-Zn battery displayed a stable and optimal potential of 1.36 V for 41 h. By normalizing the energy output to the weight of dissipated Zn, the calculated specific capacity and energy density were estimated to be 780 mAh g⁻¹ and 956 Wh kg⁻¹, respectively, markedly higher than those of Pt/C-RuO₂ (Figure S19). Also, the small chargedischarge voltage gap of the NCAc-Zn/Fe-Zn battery in Figure 5e indicates excellent rechargeability (Figure S20). Impressively, the battery also delivers a stable potential plateau in the charge-discharge test at the constant current density of 10 mA cm⁻² during prolonged operation. After 1100 continuous charge-discharge cycles (400 s for each cycle), the NCAc-Zn/Fe-Zn battery still afforded a high round-trip efficiency of 59% and a narrow discharge-recharge voltage gap of 0.79 V, much better than those of Pt/C-RuO₂ and other leading oxygen electrocatalysts reported in recent literature (Figure 5f).[5, 11, 37-40] Taken together, these results demonstrate that the NCAczn/Fe aerogels derived from biomass hydrogels can be used as high-performance bifunctional oxygen electrodes for Zn-air batteries, thanks to its high open-circuit voltage, large power density, and superb durability.

3. Conclusion

In this study, a facile, scalable strategy was developed for the preparation of nanowrinkled carbon aerogels embedded with FeN $_{\rm x}$ active sites by utilizing biomass hydrogels as the precursors and reactors. The resulting nanowrinkled carbon aerogels (NCAc-zn/Fe) showed an excellent and reversible ORR/OER electrocatalytic performance with a low voltage gap of only 0.71 V for oxygen electrocatalysis. With the obtained carbon aerogels as the (air) cathode catalysts of a Zn-air battery, the battery exhibited a higher open-circuit voltage, greater power density, and superior durability than that based on a mixture of commercial Pt/C-RuO $_{\rm 2}$ catalysts. First-principles calculation showed that FeN $_{\rm x}$ sites in Stone-Wales defect formed by the carbon nanowrinkles were most likely responsible for the excellent electrocatalytic activity. Results from the present study suggest that creating structural distortion of metal sites in carbon matrices can be exploited as an effective strategy for the design and engineering of advanced electrocatalysts based on atomically dispersed metal centers.

4. Materials and Methods

4.1 Reagents

Potassium hydroxide (KOH), iron(II) chloride tetrahydrate (FeCl₂·4H₂O), SiO₂ nanoparticles (15 nm), zinc(II) acetate (Zn(OAc)₂), potassium thiocyanate (KSCN), gelatin, and agar were purchased from Aladdin Reagents (Shanghai, China). Perchloric acid (HClO₄) and ammonium hydroxide (NH₄OH) were purchased from Xiya Reagents (Chengdu, China). Chitosan and Nafion solution were purchased from Sigma-Aldrich (America). Commercial Pt/C (20 wt %) and high purity zinc plate (99.999%) were obtained from Johnson Matthey. Polytetrafluoroethylene (PTFE, 60 wt %, D-210C) was purchased from Japan DaJin. All other reagents were analytical grade, and ultrapure water (MillQ, 18.3 M Ω cm) was used throughout this study.

4.2 Instrumentation

TEM studies were carried out with a T20 FEI TECNA1 G2 instrument. Scanning electron microscopy images were obtained with a Hitachi S-4800 field-emission scope. STEM with EDS studies were performed on a JEOL JEM-ARM200CF with aberrationcorrected STEM. Topography, maximum force, adhesion force, and current flow were measured using the Fast Force mapping technique from an Oxford Instruments Asylum Cypher S AFM housed in an Ar gas filled glove box. Raman spectra were acquired with a Renishaw inVia Raman Microscope. CD spectra were recorded onJasco-815 CD spectrometer (Japan). UV-vis spectra were obtained at Shimadzu UV-2450 spectrometer (Japan). ICP-OES studies were performed on a SPECTRO BLUE SOP instrument. XRD and XPS measurements were carried out at a D/max 2550 X-ray Power Diffractometer and a Thermo Fisher-VG Scientific ESCALAB 250Xi X-ray Photoelectron Spectrometer, respectively. N₂ adsorption-desorption isotherms were obtained with a Micromeritics ASAP 2020 surface area and porosity analyzer. Fe Kedge EXAFS measurements were performed at the Quick-EXAFS beamline of the Taiwan Photon Source in transmission mode, and the results are analyzed by using the FeN_xC_y structural model with the Athena program. An RST 5200F electrochemical workstation (Zhengzhou, China) was used to perform the voltammetric measurements. Rotating disk electrode (RDE, Pine Research Instrument) tests were carried out at the rotation rates of 400 to 1600 rpm.

4.3 Synthesis of Catalysts

In a typical reaction, 60 mg of chitosan (CS), 40 mg of SiO₂ nanoparticles (15 nm) and 2.56 ml of acetic acid (1%) were placed in screw-cap vial under magnetic stirring for 90 min, into which was added 90 μ L of NH₃H₂O (20 wt%) to adjust the solution pH to 7.0. 200 μ L of 0.2 M Fe-phenanthrolene (Fe(PM)₃²⁺) and 80 μ L of 1 M zinc acetate (Zn(OAc)₂) were then added into the above solution under stirring. Sonication treatment for 6 min yielded a hydrogel, which was denoted as CS_{Si-Zn}/FePM ("Si", "Zn" and "FePM" stand for SiO₂ nanoparticles, Zn²⁺ ions and Fe(PM)₃²⁺, respectively). The CS_{Si-Zn}/FePM hydrogel obtained above was freeze-dried and then heated to 900 °C at the heating rate of 5 °C min⁻¹ in an Ar atmosphere (containing 3% H₂). After heating at 900 °C for 3 h, the sample was cooled down to room temperature and subject to HF etching to remove SiO₂ nanoparticles, affording Fe,N-codoped carbon aerogel, which was referred to as NCA_{C-Zn}/Fe.

Three control samples were prepared in the same fashion except that only one or two of the starting materials (SiO_2 nanoparticles, Zn^{2+} ions and $Fe(PM)_3^{2+}$) were used to prepare the biomass hydrogel precursors (i.e., CS_{Si} , CS_{Si} /Fe and CS_{Si} /FePM). The corresponding aerogels were denoted as CA_C , CA_C /Fe and NCA_C /Fe, respectively.

Other experimental and theoretical details are included in the Supporting Information.

4.4 Electrochemistry

Electrochemical tests were carried out in a three-electrode electrochemical cell with a graphite rod as the counter electrode and an Ag/AgCl (saturated KCl) electrode as the reference electrode. The Ag/AgCl reference electrode was calibrated against a reversible hydrogen electrode (RHE) and all potentials in the present study were referenced to this RHE. To prepare a catalyst ink, 3 mg of the catalysts obtained above was dispersed in a 475 µL mixed solvent of H₂O and ethanol (v:v=1:1) and 25 µL of a Nafion solution (5%) under sonication for 1 h to form a homogeneous dispersion (6 mg mL⁻¹). The catalyst ink was loaded onto a cleaned glassy carbon electrode at the catalyst loading of 250 µg cm⁻² for cyclic voltammetry and 400 µg cm⁻² for RDE and RRDE measurements, respectively.

In RDE measurements the disk current density (/) is defined by the Koutechy-Levich (K-L) equation,

$$\frac{1}{J} = \frac{1}{J_L} + \frac{1}{J_K} = \frac{1}{B\omega^{1/2}} + \frac{1}{J_K} \tag{1}$$

$$B = 0.2 \text{nF} C_0(D_0)^{2/3} v^{-1/6}$$
(2)

where J_L is the limiting current density, J_K is the kinetic current density, ω is the rotation rate, n is electron transfer number, F is the Faraday's constant (96485 C mol⁻¹), C_0 is the O_2 concentration in the electrolyte solution ($1.2 \times 10^{-6} \text{ mol cm}^{-3}$); v is the kinematic viscosity of the electrolyte (0.01 cm² s⁻¹ for 0.1 M KOH). J_K can be determined from the intercept of the K-L plot (J^{-1} vs $\omega^{-\frac{1}{2}}$).

In RRDE measurements, the H₂O₂ yield and electron transfer number (n) can be calculated by equation (3) and (4).

$$\%H_2O_2 = 200 \times \frac{I_r/N}{I_d + I_r/N}$$

$$n = 4 \times \frac{I_d}{I_d + I_r/N}$$
(3)

$$n = 4 \times \frac{I_d}{I_d + I_T/N} \tag{4}$$

where I_r and I_d are the ring current and disk current, respectively, and N is the collection efficiency of the ring electrode (0.37).

4.5 Fabrication of home-made Zinc-air battery

To make a zinc-air battery, a 6 M KOH solution containing 0.2 M zinc acetate was used as the electrolyte. A zinc plate was used as the anode. The air cathode was composed of three layers, i.e., a gas diffusion layer, a Ni foam layer and a catalyst layer. The Ni foam was subject to sonication treatment in 0.1 M HCl, H₂O and ethanol consecutively, and vacuum dried at 80 °C for 3 h. The catalyst layer was prepared by mixing 60 mg NCA_{C-Zn}/Fe catalyst (or the mixture of 30 mg Pt/C and 30 mg RuO₂), 10 mg acetylene black (as a conductive agent), and 30 mg PTFE emulsion. The total thickness of the cathode was ca. 0.4 mm after compression with a manual tablet machine and vacuum dried at 80 °C for 3 h.

4.6 DFT calculations

DFT calculations were carried out by Quantum ESPRESSO which is an open-source planewave code.[41] A two-dimensional supercell was built based on an 8x8 unit cell (127-129 atoms in total). For avoiding the interactions between periodic images, the vacuum at z-axis was set at 14 Å. The ultrasoft pseudopotential was adopted. [42] The kinetic and charge density cutoff were set at 40 and 200 Ry, respectively. The 2x2x1 Monkhorst-Pack K-point grids were sampled for the supercell. The total energy was converged to 10⁻³ eV for geometric relaxation. The Marzari-Vanderbilt smearing was

adopted with a smearing of $0.01~\mathrm{Ry}$.[43] The electronic energy and force were converged to $10^{-8}~\mathrm{Ry}$ and $10^{-4}~\mathrm{a.u.}$ respectively. The phonon contribution to zero-point energy and entropy was calculated based on density functional perturbation theory.[44, 45] STM calculations were carried out based on the Tersoff and Hamann approximation[46] as implemented in open source Quantum ESPRESSO package[41] at a bias of -1.0 or +1.0 V, as described in the literature.[47]

Figures

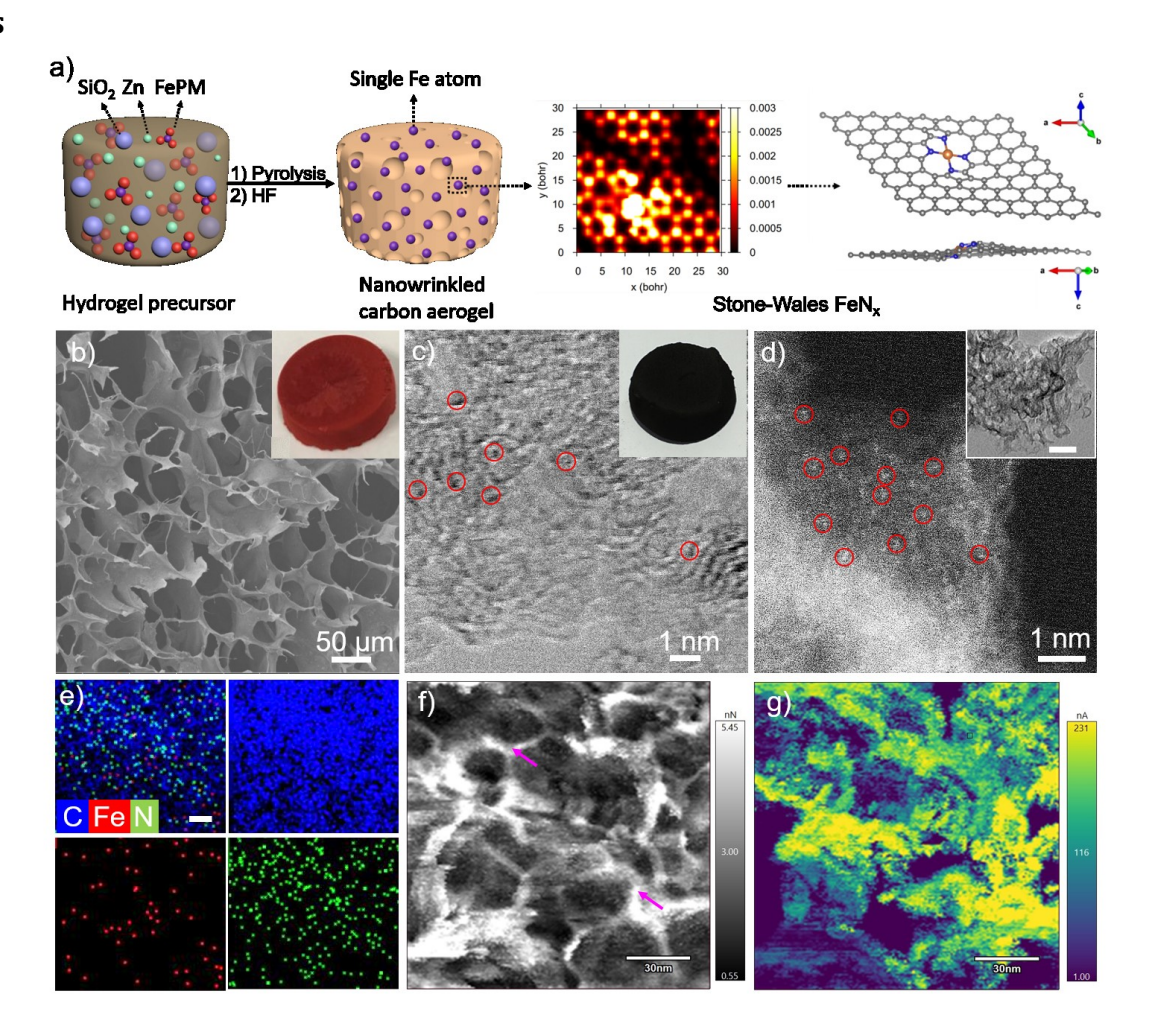


FIGURE 1 Synthesis and morphological characterization of NCA_{C-Zn}/Fe carbon aerogel. (a) Schematic representation of the synthesis of NCA_{C-Zn}/Fe carbon aerogel. (b) SEM image of the freeze-dried CS_{Si-Zn}/FePM hydrogel. Inset is a digital photo of the sample. (c) Bright-field STEM image of the NCA_{C-Zn}/Fe aerogel. Red cycles indicate single Fe atoms. Inset is a digital photo of the sample. (d) Dark-field STEM image of the NCA_{C-Zn}/Fe aerogel. Red cycles indicate single Fe atoms. Inset is a TEM image of NCA_{C-Zn}/Fe aerogel and the scale bar is 30 nm. (e) Elemental maps of NCA_{C-Zn}/Fe aerogels. The scale bar is 10 nm. AFM images of NCA_{C-Zn}/Fe aerogels: (f) adhesion force image and (g) current flow image.

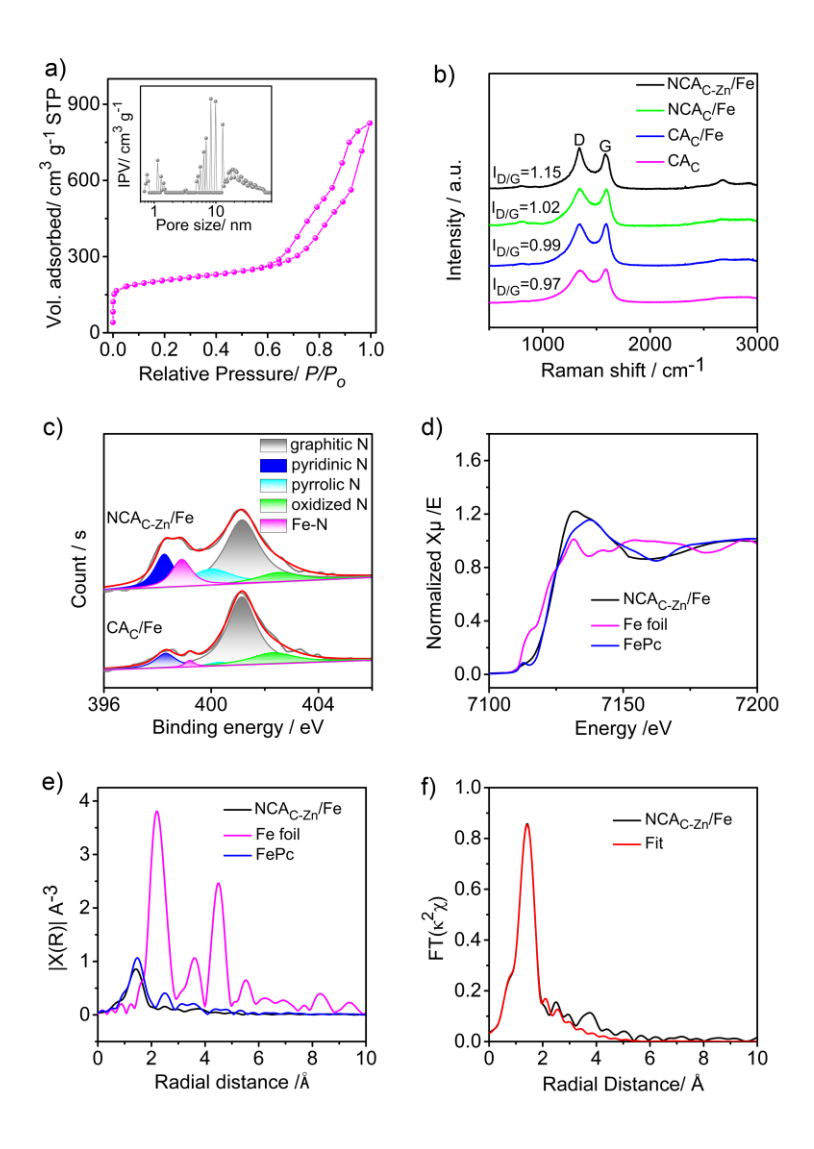


FIGURE 2 Structural characterization of NCA_{C-Zn}/Fe carbon aerogel. (a) N₂ adsorption-desorption isotherm of NCA_{C-Zn}/Fe. Inset is the corresponding pore size distribution. (b) Raman spectra of CA_C, CA_C/Fe, NCA_C/Fe and NCA_{C-Zn}/Fe. (c) XPS spectra of the N 1s electrons in CA_C/Fe and NCA_{C-Zn}/Fe. (d) K-edge XANES of NCA_{C-Zn}/Fe, FePc and Fe foil. (e) K-edge EXAFS of NCA_{C-Zn}/Fe, FePc and Fe foil. (f) The corresponding EXAFS fitting curves for the NCA_{LR}/Fe sample.

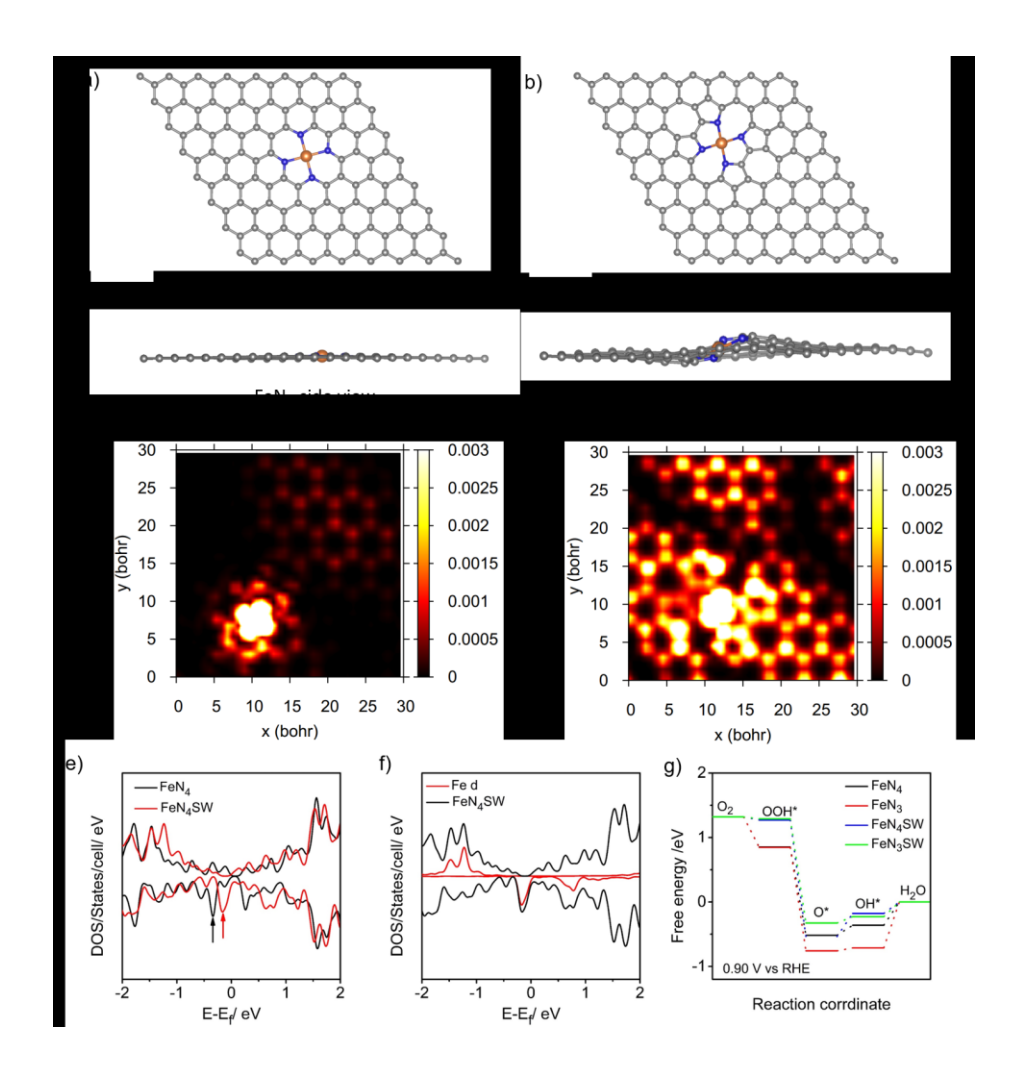


FIGURE 3 Atomic model and DOS of metal sites, Gibbs free energy diagrams of ORR. (a, c) Side/top view and simulated STM image (at a bias of -1.0 V) of normal FeN₄ doped graphene sheets. (b, d) Side/top view and simulated STM image (at a bias of -1.0 V) of Stone-Wales FeN₄ (FeN₄ SW) doped graphene sheets. (e) Density of state (DOS) of normal FeN₄ and FeN₄ SW doped graphene sheets. (f) DOS of FeN₄ SW and Fe 3d. (g) Free energy diagrams of ORR processes on normal FeN₄, normal FeN₃, FeN₄SW and FeN₃SW at the applied potential of +0.9 V vs RHE.

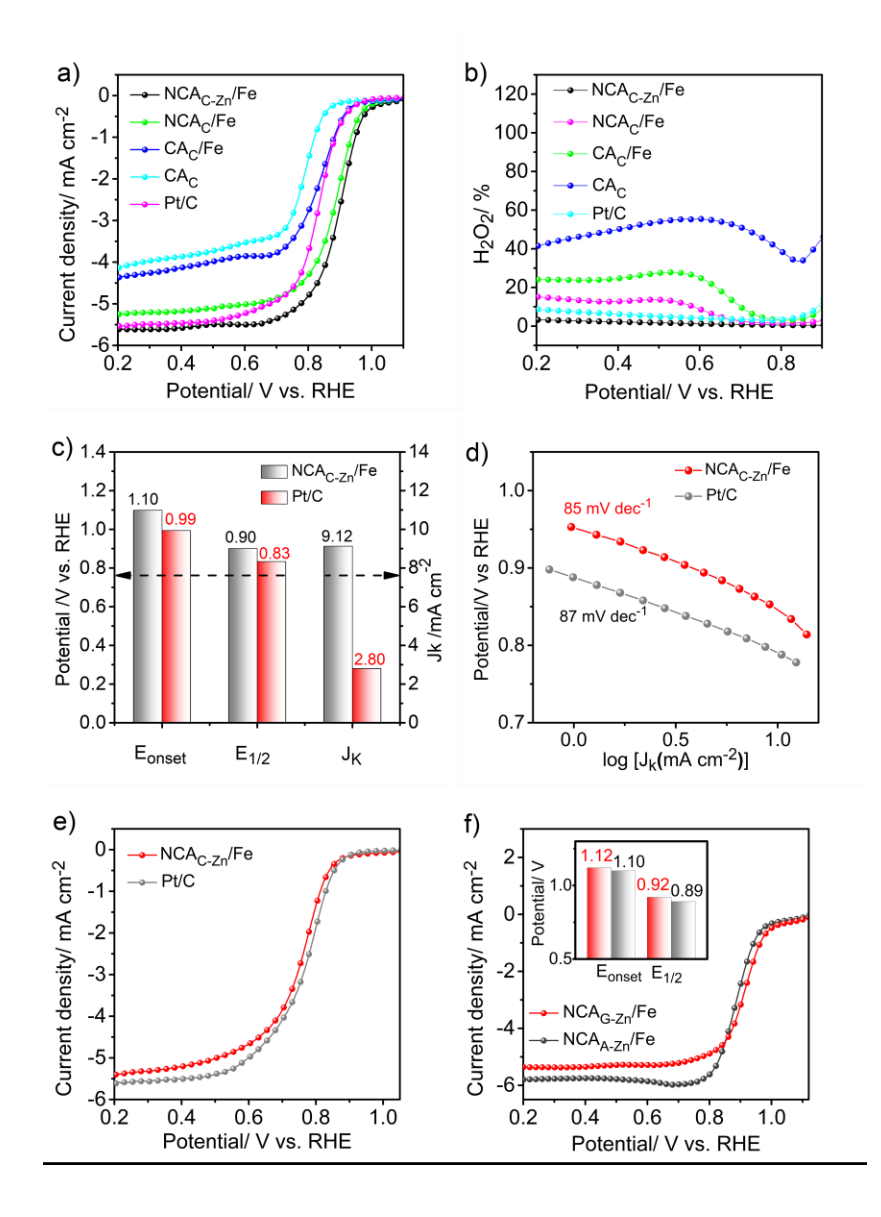


FIGURE 4 ORR performance. (a) ORR polarization curves of CA_C, CA_C/Fe, NCA_C/Fe and NCA_{C-Zn}/Fe, as well as the Pt/C at 1600 rpm in 0.1 M KOH at the potential sweep rate of 5 mV s⁻¹. (b) H₂O₂ yield of CA_C, CA_C/Fe, NCA_C/Fe, NCA_{C-Zn}/Fe and Pt/C. (c) E_{onset}, E_{1/2} and J_k (at +0.85 V) of the NCA_{C-Zn}/Fe carbon aerogels and Pt/C catalyst. (d) Tafel plots of NCA_{C-Zn}/Fe and Pt/C. (e) ORR performance in acidic media. ORR polarization curves of the NCA_{C-Zn}/Fe and the Pt/C at 1600 rpm on RDE in 0.1 M HClO₄ at the potential sweep rate of 5 mV s⁻¹. (f) ORR activity of aerogels derived from agar and gelatin hydrogels. ORR polarization curves of the NCA_{C-Zn}/Fe and NCA_{C-Zn}/Fe as well as the Pt/C at 1600 rpm on RDE in 0.1 M KOH at the potential sweep rate of 5 mV s⁻¹.

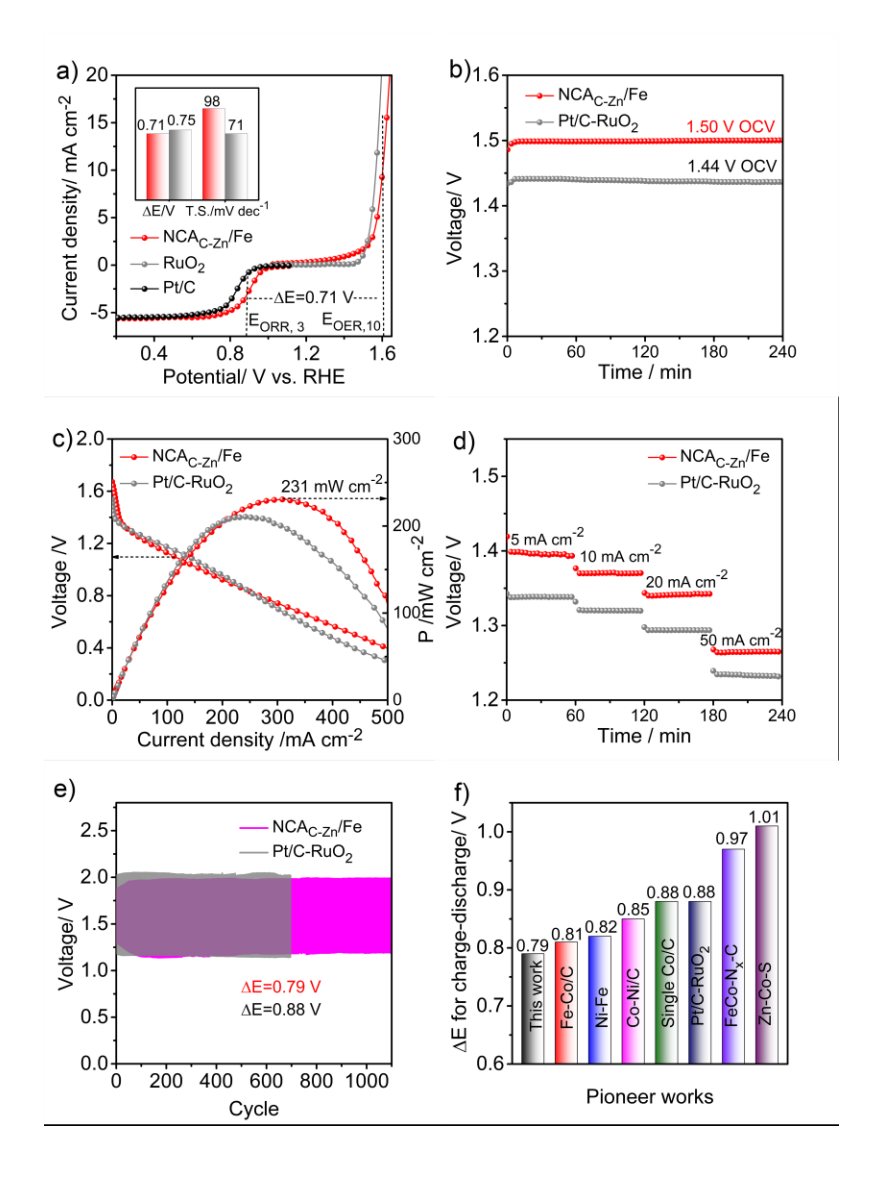


FIGURE 5 Zn-air performance tests. (a) Polarization curves for OER and ORR by NCA_{C-Zn}/Fe and Pt/C-RuO₂ in 0.1 M KOH. Inset shows the corresponding ΔE between $E_{j=3}$ and $E_{j=10}$ and Tafel slope of OER. (b) OCV and (c) power densities of Zn-air batteries assembled by NCA_{C-Zn}/Fe and Pt/C-RuO₂. (d) Discharge tests at various current densities (5, 10, 20, and 50 cm⁻²) of NCA_{C-Zn}/Fe and Pt/C-RuO₂ (e) Charge-discharge curves of Zn-air batteries assembled by NCA_{C-Zn}/Fe and Pt/C-RuO₂ at 10 mA cm⁻² for 1100 cycles (400 s per cycle). (f) Comparison of charge-discharge voltage gap for NCA_{C-Zn}/Fe with leading results reported in recent literature.[5, 11, 37-40]

Acknowledgments

Y.Z. by acknowledged support from the National Natural Science Foundation of China (21972169, 21773311, 21473257) and Hunan Provincial Science and Technology Plan Project (2017TP1001). The authors thank Dr. Yongfeng Hu in Canadian Light Source (Saskatoon) and Dr. Jeng-Lung Chen in National Synchrotron Radiation Research Center (Taiwan) for the assistance in the acquisition of XANES and EXAFS data, and Dr. Yi Peng (UCSC) for helpful discussion. T.H. is supported by a research fellowship from the China Scholarships Council (201806370027). J.V.J. acknowledged support from the Army Research Office under contract W911NF-17-1-0473. S.W.C.

acknowledged support from the National Science Foundation (CHE-1710408 and CHE-1900235).

Author Contributions:

- T. He synthesized the materials, conducted the electrochemical tests, morphological and structural characterization and wrote the paper.
- B. Lu and Y. Ping carried out the DFT calculations.
- Y. Chen and Y. Wang provided important assist in synthesis of materials and linear sweep voltammetry measurements.
- Y. Zhang performed the high angle annular dark field scanning TEM and corresponding elemental mapping measurements.
- J. L. Davenport, A. P. Chen, A. Stram, A. Mordaunt, and J. Velasco, Jr. performed the AFM studies.
- C. Pao and M. Liu provided important assist in data analysis of K-edge XANES and EXAFS.
- Z. Sun designed the experiments and revised the paper.
- Y. Zhang, and S. Chen designed experiments, analyzed data and finalized the paper (supervisors).

Conflicts of Interest

The authors declare no competing financial interests

Supplementary Materials

Table S1 BET surface area of CA_C, CA_C/Fe, NCA_C/Fe and NCA_{C-Zn}/Fe.

Table S2 EDS results of CAc, CAc/Fe, NCAc/Fe and NCAc-Zn/Fe.

Table S3 Fe contents in NCA_{C-Zn}/Fe and NCA_{C}/Fe determined by ICP-OES measurements

Table S4 Elemental analysis by XPS measurements.

Table S5 Assignments of N species for different samples.

Figure S1 Schematic illustration of the preparation of NCA_{C-Zn}/Fe carbon aerogels.

Figure S2 SEM images of CSsi, CSsi/Fe and CSsi/FePM.

Figure S3 (a) CD and (b) UV-Vis spectra of the series of biomass-derived hydrogels.

Figure S4 TEM image of NCA_{C-Zn}/Fe aerogel.

Figure S5 AFM images of NCA_{C-Zn}/Fe aerogels: (a) Topography image. (b) Max force image. (c) Adhesion force image and (d) current flow image.

Figure S6 (a) N_2 absorption-desorption isotherm and (b) pore size distribution of CA_C, CA_C/Fe, NCA_C/Fe and NCA_{C-Zn}/Fe.

Figure S7 XRD patterns of CAc, CAc/Fe, NCAc/Fe and NCAc-zn/Fe.

Figure S8 EDS profiles of CAc, CAc/Fe, NCAc/Fe and NCAc- $\rm Zn/Fe$. The results are summarized in Table S2.

Figure S9 (a) XPS of O 1s electrons of NCA_{C-Zn}/Fe . XPS of the N 1s electrons of (b) NCA_{C}/Fe and (c) CA_{C} .

Figure S10 EXAFS fitting curves for NCA $_{\text{C-Zn}}$ /Fe. Inset is the corresponding K-space profiles.

Figure S11 Top view of normal FeN_3 (a) and FeN_3 SW (b) moieties in graphene; Side view of normal FeN_3 (c) and FeN_3 SW (d) moieties.

Figure S12 Simulated STM image (at a bias of 1.0 V) of (a) normal FeN₄ (a) and (b) Stone-Wales FeN₄ (FeN₄ SW) doped graphene sheets.

Figure S13 EIS spectra of CA_C, CA_C/Fe, NCA_C/Fe and NCA_{C-Zn}/Fe.

Figure S14 RRDE polarization curves of CAc, CAc/Fe, NCAc/Fe, NCAc-Zn/Fe, as well as Pt/C at 1600 rpm on in 0.1 M KOH. Potential scan rate 5 mV s⁻¹.

Figure S15 (a) Electron transfer numbers of the biomass-derived carbon aerogels and Pt/C at different potentials. (b) Average electron transfer numbers of CA_C (4), CA_C /Fe (3), NCA_C /Fe (2), NCA_C -Zn/Fe (1) and Pt/C.

Figure S16 Durability tests of NCA_{C-Zn}/Fe and Pt/C; scan rate: 50 mV s^{-1} , medium: O₂-saturated 0.1 M KOH. (f) CV curves of the NCA_{C-Zn}/Fe and commercial Pt/C as ORR catalysts in the presence or absence of 1 M MeOH.

Figure S17 ORR polarization curves of NCA_{C-Zn}/Fe in 0.1 M KOH with or without 10 mM NaSCN.

Figure S18 OER Tafel plots of (a) NCA_{C-Zn}/Fe and (b) RuO₂.

Figure S19 Specific capacity and energy density of NCA_{C-Zn}/Fe and Pt/C-RuO₂.

Figure S20 Charge-discharge tests of NCA_{C-Zn}/Fe and Pt/C-RuO₂.

References

- [1] L. Ma, S. Chen, Z. Pei *et al.*, Single-site active iron-based bifunctional oxygen catalyst for a compressible and rechargeable zinc–air battery. *ACS Nano*, Vol. 12, no. 2, pp. 1949-1958, 2018.
- [2] S. Liu, M. Wang, X. Sun *et al.*, Facilitated Oxygen Chemisorption in Heteroatom-Doped Carbon for Improved Oxygen Reaction Activity in All-Solid-State Zinc–Air Batteries. *Advanced Materials*, Vol. 30, no. 4, pp. n/a-n/a, 2018.
- [3] Z.-Q. Liu, H. Cheng, N. Li *et al.*, ZnCo2O4 Quantum Dots Anchored on Nitrogen-Doped Carbon Nanotubes as Reversible Oxygen Reduction/Evolution Electrocatalysts. *Adv. Mater.*, Vol. 28, no. 19, pp. 3777-3784, 2016.
- [4] X.-T. Wang, T. Ouyang, L. Wang *et al.*, Redox-Inert Fe3+ Ions in Octahedral Sites of Co-Fe Spinel Oxides with Enhanced Oxygen Catalytic Activity for Rechargeable Zinc–Air Batteries. *Angew. Chem.*, Vol. 131, no. 38, pp. 13425-13430, 2019.
- [5] S. Li, C. Cheng, X. Zhao *et al.*, Active salt/silica-templated 2D mesoporous FeCo-Nx-carbon as bifunctional oxygen electrodes for Zinc–air batteries. *Angew. Chem. Int. Ed.*, Vol. 57, no. 7, pp. 1856-1862, 2018.
- [6] T. He, H. Xue, X. Wang *et al.*, Architecture of CoNx single clusters on nanocarbon as excellent oxygen reduction catalysts with high-efficient atomic utilization. *Nanoscale*, Vol. 9, no. 24, pp. 8341-8348, 2017.
- [7] T. He, X. Wang, H. Wu *et al.*, In situ fabrication of defective CoNx single clusters on reduced graphene oxide sheets with excellent electrocatalytic activity for oxygen reduction. *ACS Appl. Mater. Interfaces*, Vol. 9, no. 27, pp. 22490–22501, 2017.
- [8] B. Lu, T. J. Smart, D. Qin *et al.*, Nitrogen and iron-codoped carbon hollow nanotubules as high-performance catalysts toward oxygen reduction reaction: a combined experimental and theoretical study. *Chem. Mater.*, Vol. 29, no. 13, pp. 5617-5628, 2017.
- [9] H. Cheng, M.-L. Li, C.-Y. Su *et al.*, CuCo Bimetallic Oxide Quantum Dot Decorated Nitrogen-Doped Carbon Nanotubes: A High-Efficiency Bifunctional Oxygen Electrode for Zn–Air Batteries. *Adv. Funct. Mater.*, Vol. 27, no. 30, pp. 1701833, 2017.
- [10] D. Li, Y. Jia, G. Chang *et al.*, A Defect-Driven Metal-free Electrocatalyst for Oxygen Reduction in Acidic Electrolyte. *Chem,* Vol. 4, no. 10, pp. 2345-2356, 2018.
- [11] W. Zang, A. Sumboja, Y. Ma et al., Single Co atoms anchored in porous N-doped carbon

- for efficient zinc-air battery cathodes. ACS Catal., Vol. 8, no. 10, pp. 8961-8969, 2018.
- [12] Y. Peng, B. Lu, S. Chen, Carbon-supported single atom catalysts for electrochemical energy conversion and storage. *Adv. Mater.*, Vol. 30, no. pp. e1801995, 2018.
- [13] H. Xue, T. He, J. M. Chabu *et al.*, Iron single clusters anchored on N-doped porous carbon as superior trace-metal catalysts toward oxygen reduction. *Adv. Mater. Interfaces*, Vol. no. pp. n/a-n/a, 2018.
- [14] Y. Peng, B. Lu, L. Chen *et al.*, Hydrogen evolution reaction catalyzed by ruthenium ion-complexed graphitic carbon nitride nanosheets. *J. Mater. Chem. A*, Vol. 5, no. 34, pp. 18261-18269, 2017.
- [15] Y. Deng, B. Chi, J. Li *et al.*, Atomic Fe-doped MOF-derived carbon polyhedrons with high active-center density and ultra-high performance toward PEM fuel cells. *Adv. Energy Mater.*, Vol. 0, no. 0, pp. 1802856, 2019.
- [16] Q. Deng, J. Zhao, T. Wu *et al.*, 2D transition metal—TCNQ sheets as bifunctional single-atom catalysts for oxygen reduction and evolution reaction (ORR/OER). *J. Catal.*, Vol. 370, no. pp. 378-384, 2019.
- [17] X. Wang, Z. Chen, X. Zhao *et al.*, Regulation of Coordination Number over Single Co Sites Triggers the Efficient Electroreduction of CO2. *Angew. Chem.*, Vol. no. pp. n/a-n/a, 2017.
- [18] Y. Deng, B. Chi, X. Tian *et al.*, g-C3N4 promoted MOF derived hollow carbon nanopolyhedra doped with high density/fraction of single Fe atoms as an ultra-high performance non-precious catalyst towards acidic ORR and PEM fuel cells. *J. Mater. Chem. A*, Vol. 7, no. 9, pp. 5020-5030, 2019.
- [19] V. Budarin, J. H. Clark, J. J. E. Hardy *et al.*, Starbons: new starch-derived mesoporous carbonaceous materials with tunable properties. *Angew. Chem.*, Vol. 118, no. 23, pp. 3866-3870, 2006.
- [20] S. De, A. M. Balu, J. C. van der Waal *et al.*, Biomass-derived porous carbon materials: synthesis and catalytic applications. *Chem. Cat. Chem.*, Vol. 7, no. 11, pp. 1608-1629, 2015.
- [21] N. Sahiner, Soft and flexible hydrogel templates of different sizes and various functionalities for metal nanoparticle preparation and their use in catalysis. *Prog. Polym. Sci.*, Vol. 38, no. 9, pp. 1329-1356, 2013.
- [22] C. Lv, W. Xu, H. Liu *et al.*, 3D Sulfur and Nitrogen Codoped Carbon Nanofiber Aerogels with Optimized Electronic Structure and Enlarged Interlayer Spacing Boost Potassium-Ion Storage. *Small*, Vol. 15, no. 23, pp. 1900816, 2019.
- [23] H. Li, X. Zhao, H. Liu *et al.*, Sub-1.5 nm Ultrathin CoP Nanosheet Aerogel: Efficient Electrocatalyst for Hydrogen Evolution Reaction at All pH Values. *Small*, Vol. 14, no. 41, pp. 1802824, 2018.
- [24] Z. Sun, F. Lv, L. Cao *et al.*, Multistimuli-Responsive, Moldable Supramolecular Hydrogels Cross-Linked by Ultrafast Complexation of Metal Ions and Biopolymers. *Angew. Chem. Int. Ed.*, Vol. 54, no. 27, pp. 7944-7948, 2015.
- [25] B. Biswas, A. Al-Hunaiti, M. T. Räisänen *et al.*, Efficient and Selective Oxidation of Primary and Secondary Alcohols Using an Iron(III)/Phenanthroline Complex: Structural Studies and Catalytic Activity. *Eur. J. Inorg. Chem.*, Vol. 2012, no. 28, pp. 4479-4485, 2012.
- [26] X. Sun, G.-P. Hao, X. Lu *et al.*, High-defect hydrophilic carbon cuboids anchored with Co/CoO nanoparticles as highly efficient and ultra-stable lithium-ion battery anodes. *J. Mater. Chem. A*, Vol. 4, no. 26, pp. 10166-10173, 2016.
- [27] G.-P. Hao, G. Mondin, Z. Zheng *et al.*, Unusual Ultra-Hydrophilic, Porous Carbon Cuboids for Atmospheric-Water Capture. *Angew. Chem. Int. Ed.*, Vol. 54, no. 6, pp. 1941-1945, 2015.
- [28] S. H. Cho, S.-M. Park, Electrochemistry of Conductive Polymers 39. Contacts between Conducting Polymers and Noble Metal Nanoparticles Studied by Current-Sensing Atomic Force Microscopy. *J. Phys. Chem. B*, Vol. 110, no. 51, pp. 25656-25664, 2006.
- [29] H. J. Lee, S.-M. Park, Electrochemistry of Conductive Polymers. 30. Nanoscale

Research Manuscript Template Page 18 of 20

- Measurements of Doping Distributions and Current-Voltage Characteristics of Electrochemically Deposited Polypyrrole Films. *J. Phys. Chem. B*, Vol. 108, no. 5, pp. 1590-1595, 2004.
- [30] C. Zhu, Q. Shi, B. Z. Xu *et al.*, Hierarchically porous M-N-C (M = Co and Fe) single-Atom electrocatalysts with robust MNx active moieties enable enhanced ORR performance. *Adv. Energy Mater.*, Vol. no. pp. 1801956, 2018.
- [31] Y. Yang, Z. Lun, G. Xia *et al.*, Non-precious alloy encapsulated in nitrogen-doped graphene layers derived from MOFs as an active and durable hydrogen evolution reaction catalyst. *Energy Environ. Sci.*, Vol. 8, no. 12, pp. 3563-3571, 2015.
- [32] G. Wan, P. Yu, H. Chen *et al.*, Engineering single-atom cobalt catalysts toward improved electrocatalysis. *Small*, Vol. 14, no. 15, pp. 1704319, 2018.
- [33] R. Jiang, L. Li, T. Sheng *et al.*, Edge-site engineering of atomically dispersed Fe–N4 by selective C–N bond cleavage for enhanced oxygen reduction reaction activities. *J. Am. Chem. Soc.*, Vol. 140, no. 37, pp. 11594-11598, 2018.
- [34] W. Xia, A. Mahmood, Z. B. Liang *et al.*, Earth-abundant nanomaterials for oxygen reduction. *Angew. Chem. Int. Ed.*, Vol. 55, no. 8, pp. 2650-2676, 2016.
- [35] H. Jiang, Y. Liu, W. Z. Li *et al.*, Co nanoparticles confined in 3D nitrogen-doped porous carbon foams as bifunctional electrocatalysts for long-life rechargeable Zn-air batteries. *Small*, Vol. 14, no. 13, pp. 2018.
- [36] S. Liu, M. Wang, X. Sun *et al.*, Facilitated oxygen chemisorption in heteroatom-doped carbon for improved oxygen reaction activity in all-solid-state zinc—air batteries. *Adv. Mater.*, Vol. 30, no. 4, pp. 1704898, 2018.
- [37] X. Wu, X. Han, X. Ma *et al.*, Morphology-controllable synthesis of Zn–Co-mixed sulfide nanostructures on carbon fiber paper toward efficient rechargeable zinc–air batteries and water electrolysis. *ACS Appl. Mater. Interfaces*, Vol. 9, no. 14, pp. 12574-12583, 2017.
- [38] W. Niu, S. Pakhira, K. Marcus *et al.*, Apically dominant mechanism for improving catalytic activities of N-doped carbon nanotube arrays in rechargeable zinc–air battery. *Adv. Energy Mater.*, Vol. 8, no. 20, pp. 1800480, 2018.
- [39] K. Fu, Y. Wang, L. Mao *et al.*, Rational assembly of hybrid carbon nanotubes grafted on the carbon nanofibers as reliable and robust bifunctional catalyst for rechargeable zinc-air battery. *J. Power Sources*, Vol. 421, no. pp. 68-75, 2019.
- [40] Y. Fan, S. Ida, A. Staykov *et al.*, Ni-Fe nitride nanoplates on nitrogen-doped graphene as a synergistic catalyst for reversible oxygen evolution reaction and rechargeable Zn-air battery. *Small*, Vol. 13, no. pp. 1700099, 2017.
- [41] P. Giannozzi, S. Baroni, N. Bonini *et al.*, QUANTUM ESPRESSO: a modular and open-source software project for quantum simulations of materials. *J. Phys.: Condens. Matter*, Vol. 21, no. 39, pp. 395502, 2009.
- [42] K. F. Garrity, J. W. Bennett, K. M. Rabe *et al.*, Pseudopotentials for high-throughput DFT calculations. *Comput. Mater. Sci.*, Vol. 81, no. pp. 446-452, 2014.
- [43] N. Marzari, D. Vanderbilt, A. De Vita *et al.*, Thermal contraction and disordering of the Al(110) surface. *Phys. Rev. Lett.*, Vol. 82, no. 16, pp. 3296-3299, 1999.
- [44] S. Baroni, S. de Gironcoli, A. Dal Corso *et al.*, Phonons and related crystal properties from density-functional perturbation theory. *Rev. Mod. Phys.*, Vol. 73, no. 2, pp. 515-562, 2001.
- [45] Y. Li, G. Galli, Electronic and spectroscopic properties of the hydrogen-terminated Si(111) surface from ab initio calculations. *Phys. Rev. B*, Vol. 82, no. 4, pp. 045321, 2010.
- [46] J. Tersoff, D. R. Hamann, Theory and Application for the Scanning Tunneling Microscope. *Phys. Rev. Lett.*, Vol. 50, no. 25, pp. 1998-2001, 1983.
- [47] S.-O. Guillaume, B. Zheng, J.-C. Charlier *et al.*, Electronic properties and STM images of doped bilayer graphene. *Phys. Rev. B*, Vol. 85, no. 3, pp. 035444, 2012.

Research Manuscript Template Page 19 of 20